

# A fusion relevant data-driven engineering void swelling model for 9Cr tempered martensitic steels

Takuya Yamamoto, G. Robert Odette\*

University of California Santa Barbara, Santa Barbara, 2355 Engineering II Bldg., Santa Barbara, CA 93106, United States

## ARTICLE INFO

### Article history:

Received 10 May 2022

Revised 2 September 2022

Accepted 11 October 2022

Available online 14 October 2022

### Keywords:

Void swelling

helium effects

Irradiation damage

9Cr tempered martensitic steel

Fusion materials

## ABSTRACT

The UCSB database on cavity evolution in 9-12Cr tempered martensitic steels (TMS), includes the results for both dual heavy and helium ion (DII), and High Flux Isotope Reactor (HFIR) in situ helium injection (ISHI) neutron irradiations at 500°C. These results were combined with literature single ion and fission neutron irradiation data to derive a model for the void volume fraction,  $f_v$ , as a function of displacements per atom (dpa) and transmutant helium concentrations in atomic parts per million (appm). The scientific foundation for the paper is described in a companion paper entitled “*Cavity Evolution and Void Swelling in Dual Ion Irradiated Tempered Martensitic Steels*”. Here, we show that  $f_v$ (dpa, He/dpa) is described by the incubation dose,  $dpa_i$ , for the onset of void growth, and the post-incubation growth rate,  $f_v'$ (%/dpa). Both  $dpa_i$  and  $f_v'$  decrease with increasing He/dpa at  $> \sim 5$ . The  $dpa_i$  is also lower for the ISHI neutron irradiations at the same He/dpa. Single heavy ion and fission reactor neutron irradiations, with low He/dpa ratios, have a much larger  $dpa_i$ . Based on a combined analysis of DII, single ion, ISHI and fission neutron data, we further show that the post-incubation  $f_v$  data analyzed here have a common empirical curve shape, with  $f_v'$  reaching up to  $\sim 0.2\%/dpa$  at very high dpa. We also show that  $f_v'$  can be predicted based on a physical model of defect partitioning between evolving sinks. At 500°C and fusion relevant He/dpa  $\approx 10$ , the best-fit model predicts nominal swelling,  $S = f_v/(1-f_v)$ , of  $\sim 1.1$ , 4.9 and 16% at 50, 100 and 200 dpa, respectively. The physically motivated, data-driven model includes estimated uncertainties for both  $dpa_i$  and  $f_v'$ .

© 2022 Elsevier B.V. All rights reserved.

## 1. Introduction and background

Fusion reactor designs must account for dimensional instabilities in structural components associated with void swelling, as well as thermal and irradiation creep [1]. It is well established that high He/dpa levels can cause severe degradation of both mechanical properties and acceleration of void swelling in 9-12Cr tempered martensitic steels (TMS) [2]. Thus, irradiation damage in a He-rich environment may greatly narrow the service window of the current candidate TMS for fusion reactor first wall and blanket structures [2].

Void swelling in fast neutron irradiated austenitic stainless steels was first reported by Cawthorne and Fulton in 1967 [3]. Swelling was the subject of intense international research for several following decades. A review of this vast literature is beyond the scope of this paper, which focuses on much more swelling-resistant TMS. Earlier research showed that swelling is generally manifested in three stages [2,4–15]: a) an incubation stage of the stable growth of gas bubbles by the addition of helium atoms,

but with negligible swelling; b) a transient stage, associated with an increasing fraction of the stably growing bubbles converting to unstably growing voids beyond a critical size at an incubation  $dpa_i$ , due to an excess vacancy flux to void sinks; and, c) a quasi-steady-state swelling rate stage, associated with growing voids, with roughly balanced void and interstitial-biased dislocation sink strengths and a small net dislocation interstitial bias. Note, a steady-state swelling regime is not always observed, and decreases in rates with sink imbalances that increase with dpa are also possible [8].

The incubation stage is sensitive to many material and irradiation variables, such as alloy composition and starting microstructure, dpa rate (dpa'), irradiation temperature (T), the bubble microstructure initially formed, and, especially, the He/dpa ratio (appm He/dpa). The transient stage is somewhat less sensitive to these variables, while the steady state is least sensitive, typically eventually, reaching an approximately common swelling rate, such as the nominal  $f_v' \approx 1\%/dpa$  in austenitic stainless steels, as proposed by Garner et al. [16]. A key observation, based on a large body of data, is that helium is an essential ingredient in void swelling at low neutron irradiation dpa rates. However, very high He/dpa can suppress swelling due to the formation of sta-

\* Corresponding author.

ble bubble-dominated microstructures, which resist conversion to voids and reduce post-incubation swelling rates [2,5-12,14,17,18].

Quasi-steady-state swelling can be understood in terms of simple partitioning of defects between the sinks, with an excess flux of vacancies accumulating at voids, while an excess flux of self-interstitial atoms goes to biased dislocations [2,4-14,17-18]. Bubble sinks effectively act as vacancy-interstitial recombination centers, which decrease swelling [2, 19]. The distribution of helium to a larger number of small bubbles suppresses their conversion to voids both directly, and due to a lower effective vacancy supersaturation, associated with a high bubble sink density [2]. While, for a number of reasons, bcc TMS are much more swelling resistant than fcc austenitic stainless steels, they generally behave in a qualitatively similar manner [2,13,18], and many other references cited therein.

For low He conditions, TMS have much larger incubation dpa<sub>i</sub>, and lower steady-state swelling rates [1,13,19], like the nominal value of  $f_v' \approx 0.2\%/dpa$  proposed by Garner et al. [16]. Note,  $f_v'$  actually evolves, consistent with the physical defect partitioning model described in Section 4. The larger dpa<sub>i</sub> in TMS versus austenitic stainless steels is due to lower (and initially negative) dislocation bias for self-interstitials [20-24], higher self-diffusion rates in bcc versus fcc lattices [13], lower He generation rates, and higher sink densities and helium trapping sites [25]. The lower  $f_v'$  is mainly due to lower net dislocation interstitial bias in bcc alloys [20,23,24]. Note, however,  $f_v'$  is also sensitive to the He/dpa ratio, which affects the relative sink strengths of bubbles, voids, and dislocations. As noted above, a high He/dpa can lead to a large persistent population of bubbles which can significantly reduce  $f_v'$  [2, 5-12,14,17-18].

We have previously demonstrated that the in situ He injection (ISHI) technique in mixed spectrum fission reactor irradiations, like in the High Flux Isotope Reactor (HFIR), provides a very attractive approach to assessing the effects of He-dpa synergisms, while avoiding most of the confounding effects associated with Ni- or B-doping type experiments [2,26-33]. Another approach to study He-dpa synergisms is to use dual ion irradiations (DII) to simultaneously implant He, while creating displacement damage with heavy ions [2,34-37]. Although 9Cr TMS are much more resistant to swelling than austenitic stainless steels, especially under low He neutron and single ion irradiation conditions, there is increasing evidence that these alloys can swell significantly at fusion-relevant He levels, and at sufficiently high single ion irradiation dpa [34,38-44].

Here, we use our ISHI [2,28,30,32-33] and DII results [34], supplemented by literature single ion and neutron irradiation databases [16,38-41,45-56], to develop a quantitatively predictive engineering model for void swelling ( $f_v$ ) in TMS for fusion service relevant dpa, dpa rate (dpa'), He and He/dpa (in units of appm/dpa). Strictly speaking, the treatment of He/dpa in the model is for 500°C irradiations. Still, it may tentatively provide reasonable  $f_v$  estimates over a wider range of swelling temperatures from ~400 to 500°C, as discussed in [34].

## 2. Materials and methods

Details of the analysis of our ISHI neutron and DII database underpinning the swelling model can be found in [28,30,32-34]. Here, we extend the analysis to higher post-incubation dpa based on integrating the ISHI neutron irradiation and DII data, with lower He neutron and single ion irradiation results in the literature [16,38-41,45-56]. Note, the experimental results and analysis in a companion paper on DII are especially pertinent to the model developed here [34].

**Materials:** The materials used in the ISHI and DII studies are 9Cr TMS, including two heats of F82H and the reference heat Euro-

fer97 [28-30,34-37] in the as-tempered condition. The composition of the most widely studied large International Energy Agency (IEA) heat of F82H (IEA) is: 7.5Cr, 2W, 0.2V, 0.1C, 0.1Si, 0.02Ta (wt%), and 60 wppm N [57]. Another variant of F82H, known as Mod.3 (M3), reduced the N and Ti to 14 wppm and 0.001%, respectively, while increasing Ta to 0.1% [58]. The F82H M3 was also irradiated in the 20% cold-worked condition, but the corresponding data is not included in this analysis. The composition of Eurofer97 (E97) is: 8.93Cr, 1.08W, 0.49Mn, 0.20V, 0.12C, 0.04Si, 0.021N, < 0.01(P, Cu, Co, Ti, Nb, B), bal. Fe (wt%) [59]. The corresponding heat treatments were: a) IEA: austenitizing at 1040°C for 40 min, followed by normalizing (air-cooling), with a final tempering treatment at 750°C for 1 h [57]; and, b) M3: austenitizing at 1040°C for 30 min, followed by normalizing (air-cooling), with a final tempering treatment at 740°C for 1.5 h [58]; and, c) E97: austenitizing at 980°C for 30 min, followed by normalizing (air-cooling), with a final tempering treatment at 760°C for 1.5 h [59]. More details of the steels can be found in [57-59].

**Irradiations:** University of California Santa Barbara (UCSB) has been developing a microstructure database based on two types of irradiations resulting in high dpa and He accumulation. One is the ISHI method in mixed spectrum fission reactor irradiations, using Ni-bearing implanter layers to inject high-energy  $\alpha$ -particles into an adjacent material that is simultaneously undergoing fast neutron-induced displacement damage, as illustrated in Figure 1a [2,26,27]. A series of ISHI irradiation experiments have been carried out in the mixed spectrum HFIR reactor [26-33]. Micron-scale NiAl injector coatings uniformly injected  $\alpha$ -particles to a depth of ~5 to 8  $\mu\text{m}$  in transmission electron microscopy (TEM) discs for a large matrix of alloys irradiated over a range of temperatures and dpa at controlled He/dpa ratios ranging from < 1 to ~65. The other approach is to use DII to simultaneously implant He while creating displacement damage with heavy ions [34-37]. The DII were performed in DuET facility at the Institute of Advanced Energy, Kyoto University in Japan. Here,  $\text{Fe}^{3+}$  and  $\text{He}^+$  ions are accelerated to 6.4 MeV and 1 MeV, respectively, to create the dpa damage and He profiles, as illustrated in Figure 1b. The  $\text{He}^+$  ion beam passes through a rotating energy degrader foil with varying thicknesses to create four ion energies and corresponding He ranges, resulting in a broader and relatively uniform He/dpa deposition profile up to a maximum depth of ~1100 nm. The ion beams are rastered in DuET. The two yellow bands in Figure 1b at 600±50 nm and 1050±50 nm mark the range of average irradiation condition locations for the various experiments listed in Table 1, at a nearly constant He/dpa ratio. However, data was collected over a wider range of depths, with varying He/dpa, as discussed in [34]. Data at ≥ 1300 nm and shallower than 300 nm (black shaded regions) were generally excluded due to injected interstitial and surface effects, respectively. This restriction also eliminates regions with steep defect gradients.

Note, the ISHI and DII techniques are complementary, but manifest many differences that, in the case of DII, include, but are not limited to: a) much higher dpa rates; b) non-uniform spatial distributions of dpa; c) the proximity of a free surface; and, d) Fe ions deposited as injected self-interstitial atoms near the dpa peak [2,60] and many references therein.

**Post-irradiation examination (PIE) methods (TEM) for cavities:** In both of DII and ISHI experiments, transmission electron microscopy (TEM) specimens were prepared by focused ion beam micromachining (FIBing) at a low final current of 5.5 pA and voltage of 2 keV. The cavities were characterized using standard bright field through-focus sequence TEM imaging. More details of the PIE methods can be found in [27-28,30-35].

The updated DII cavity microstructure database used here, including newly analyzed results for 9Cr TMS F82H [34], contains data on 234 irradiation (dpa, He, dpa rate)-material condition com-

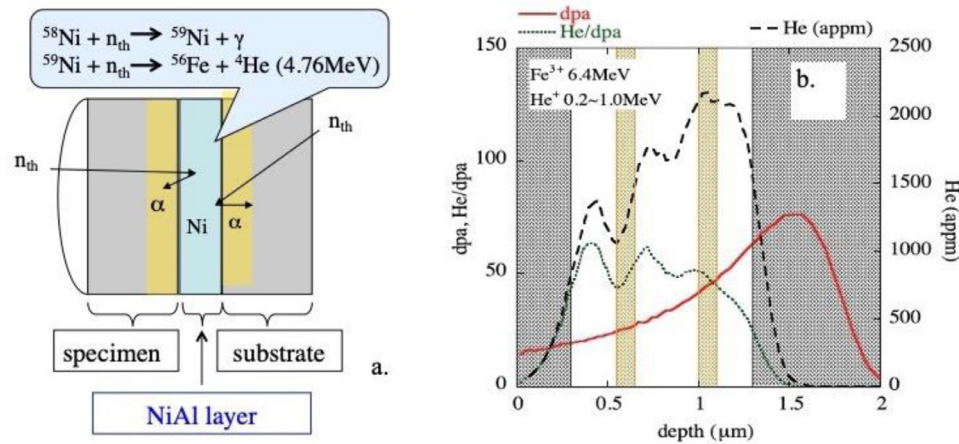


**Figure 1.** a) Schematic of in situ He injection experiments; and, b) an example of dpa, He, and He/dpa profiles in the DuET experiments. The two yellow bands in Figure 1b at  $600 \pm 50$  nm and  $1050 \pm 50$  nm mark the range of average irradiation condition locations for the various experiments listed in Table 1, at a nearly constant He/dpa ratio. The black shaded regions,  $\text{depth} \geq 1300$  nm and  $\leq 300$  nm, were where data are generally excluded due to injected interstitial and surface effects, respectively.

**Table 1**  
The nominal dpa-He conditions of DII and ISHI experiments

Irr. Type	Irr. ID	T (°C)	Nominal Condition				DII at Peak He			Alloys	Specimen ID
			dpa	He (appm)	He/dpa	dpa/s	dpa	He (appm)	He/dpa		
Dual ion irradiation	DI10B1	500	26	1210	47	$5.0 \times 10^{-4}$	45	2100	47	M3	N/A
	DI10B2	500	9.9	457	46	$5.2 \times 10^{-4}$	17	795	46	M3	N/A
	DI10B3	500	10	480	47	$5.1 \times 10^{-4}$	18	840	47	M3	N/A
	DI13A	500	26	390	15	$5.1 \times 10^{-4}$	44	670	15	IEA; M3	N/A
	DI13B1	500	30	848	29	$1.5 \times 10^{-3}$	51	1467	29	IEA; M3	N/A
	DI14A1	500	30	1200	47	$1.3 \times 10^{-3}$	45	2100	47	IEA; M3	N/A
	DI14B	500	45	1290	28	$8 \times 10^{-4}$	79	2230	28	IEA; M3	N/A
	DI15A1	500	51	1360	27	$8.6 \times 10^{-4}$	88	2350	27	IEA; M3	N/A
	DI16A	500	51.5	2330	45	$6.5 \times 10^{-4}$	89.2	4020	45	IEA; M3	N/A
Neutron irradiation (ISHI)	DI16A+19A	500	82	3750	45	$6.5 \times 10^{-4}$	142	6400	45	IEA; M3	N/A
	JP26	500	9	169	18.8	$9 \times 10^{-7}$	N/A			E97	R25
	JP26	500	9	190	21.1	$9 \times 10^{-7}$	N/A			M3	H24
	JP26	500	9	372	41.3	$9 \times 10^{-7}$	N/A			E97	R26
	JP26	500	9	372	41.3	$9 \times 10^{-7}$	N/A			E97	R27
	JP26	500	9	380	42.2	$9 \times 10^{-7}$	N/A			M3	H27
	JP27	500	21	510	24.3	$9 \times 10^{-7}$	N/A			E97	H57b
	JP27	500	21	1230	58.6	$9 \times 10^{-7}$	N/A			E97	R56

binations, including: a) 136 conditions for as-tempered M3 heat; and, b) 98 conditions for as-tempered IEA heat. Table 1 summarizes nominal conditions for the DII at two depths, and the ISHI, again all at 500°C [28,30,32,34–37].

**Injected interstitial effects:** As noted previously, there are a number of differences, and confounding factors, between neutron (including ISHI) and ion (single and dual) irradiations [2,60] and many references therein. Most notably, ion irradiations: (a) have dpa rates that are generally from 2 to 4 orders of magnitude larger than in high flux neutron irradiations; (b) have atomic recoil spectra with lower energies than in neutron irradiations; (c) experience dpa gradients and time-dependent (pulsed) dpa rates in the case of ion beam rastering; (d) can undergo C contamination; (e) can be influenced by surface sink effects; and, f) be subject to internal stresses. However, an even more important difference is due to the injected interstitial atoms in ion irradiations.

Significant injected interstitial effects have been observed in many experimental studies [34,61,62] and those cited in [34], and they have been extensively modeled [63–67]. Both the observations, and rate theory model predictions, show that back diffusion of injected interstitials suppresses swelling at distances of up to  $\approx 600$  nm, or more, behind the ion deposition peak. The strong injected interstitial effect is due to a further reduction in the slight differences between vacancy and interstitial (self and in-

jected) fluxes to cavity sinks. The predicted effects are largest on void nucleation, consistent with experimental observations [62,66]. The combination of surface sink and injected interstitials can lead to double peaks in the swelling as a function of depth [66]. For example, in an injected interstitial effects study of unalloyed Fe, the swelling peaks were at  $\sim 600$  nm behind the ion deposition peak and  $\sim 200$  nm away from the surface, between  $\sim 200$  and  $600$  nm [62,66]. The use of very high-energy ions reduces injected interstitial effects, but to date, there is not much published swelling data from such studies. Fortunately, as shown in a companion paper [34], local microstructures can also mitigate injected interstitial effects, by blocking the interstitial defect back flux. The injected interstitial shielding features include boundaries and walls of large carbides [34]. We hypothesize that nearly intrinsic swelling rates can be observed in these locally shielded regions. More generally, we assume that the maximum cavity volume fraction observed in the DII, can be used to establish a nominally intrinsic  $f_v'$  as a function of He/dpa. As shown in [34], these data are consistent with simple defect partitioning mechanisms mediating the post-incubation  $f_v'$  [2].

Ignoring vacancy emission from voids, the  $f_v'$  is controlled by the combination of system interstitial bias, here simply attributed to dislocations, and the relative defect sink strengths of bubble, voids, and dislocations. The excess vacancies are collected at voids,

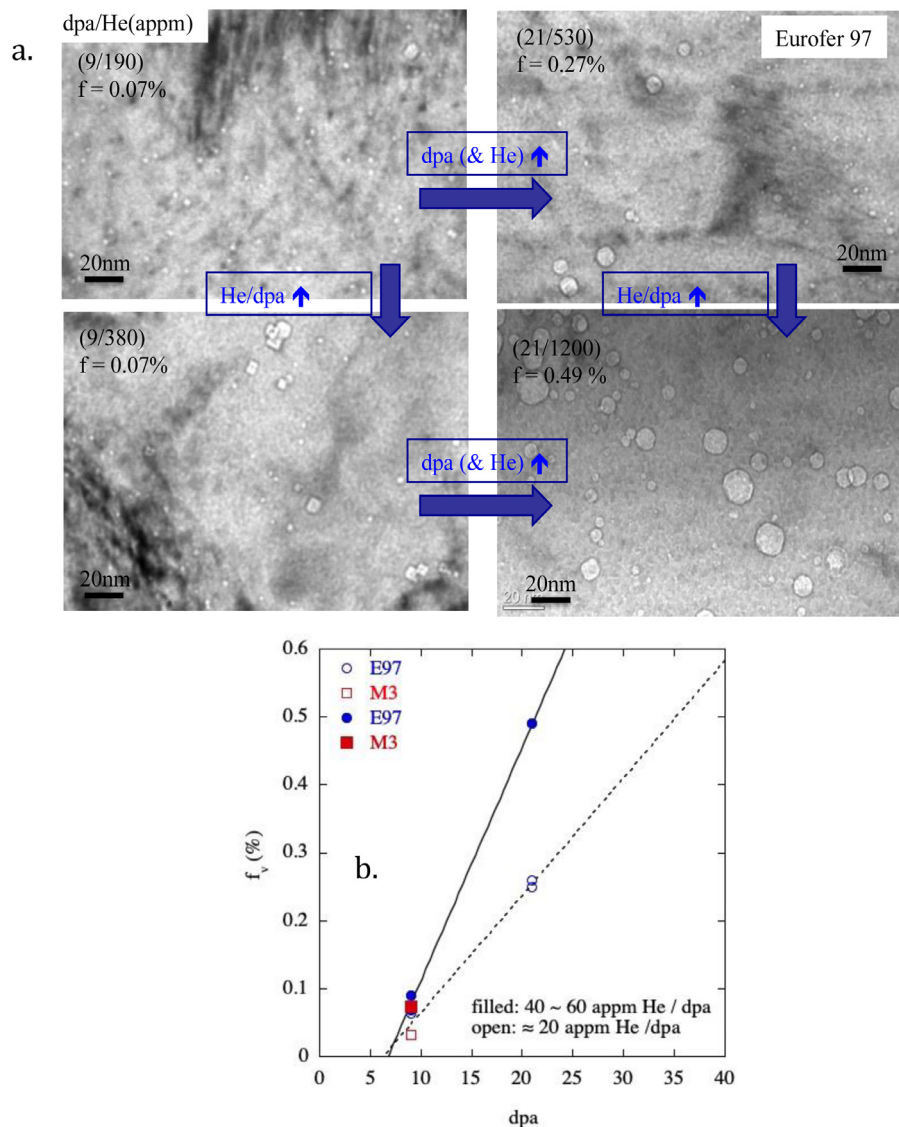


**Figure 2.** a) The ISHI cavity microstructure in a TMS Eurofer 97 steel from dpa/He = 9/190 (top left) to higher He/dpa 9/380 (bottom left), to higher dpa and He/dpa 21/530 (top right) to high He/dpa 21/1200 (bottom right); and, b) the corresponding  $f_v$  as a function of dpa and linear least square fits to estimate incubation  $dpa_i$  and  $f_v'$ .

taken here to be cavities with diameters  $> 4$  nm. A detailed scanning TEM (STEM) study measured the dislocation, bubble, and void densities (sink strengths) in the same region and strongly supports the sink partitioning hypothesis [34].

### 3. Cavity evolution

**ISHI data:** The ISHI microstructure database includes 7 dpa and He as-tempered (AT) irradiation conditions at 500°C. Figure 2a illustrates the evolution of the cavity microstructure in a TMS E97 steel from the lowest dpa and He/dpa at dpa/He = 9/190 condition (top left), to higher He/dpa 9/380 (bottom left), to higher dpa 21/580 (top right), and higher appm He 21/1200 (bottom right) [32,33]. The ISHI data clearly show that high He/dpa accelerates void nucleation, resulting in a lower  $dpa_i$ . Figure 2b plots  $f_v$  as a function of dpa, showing a higher  $f_v'$  at higher He/dpa. The estimated  $dpa_i$ , found by back extrapolating the swelling data to  $f_v = 0$ , are similar at  $\sim 6.5$  dpa over the He/dpa range from  $22 \pm 4$  to  $50 \pm 10$ . The individual  $f_v$  errors are estimated to be  $\sim \pm 10\%$ , mainly from the thickness uncertainties; however, the individual data point error estimates do not affect the fitting parameters and

corresponding uncertainties, which are  $dpa_i = 6.3 \pm 0.9$  and  $6.8 \pm 0.2$ , and  $f_v' = 0.017 \pm 0.001$  and  $0.034 \pm 0.001$ , at 22 and 50 He/dpa, respectively. The low  $dpa_i$  for high He/dpa ISHI neutron irradiation conditions are consistent with the predictions of a multi-scale master model of He transport, fate, and consequences as discussed in [68,69] and Supplemental Information SI2. Unfortunately, the ISHI data is probably too limited to provide highly reliable  $f_v'$  fits.

**DII data:** A detailed mechanistic analysis of the He/dpa dependence of  $dpa_i$  and the post-incubation  $f_v'$  can be found in [34], which will not be repeated here. Figure 3 summarizes the key results. Figures 3a and b show the high  $f_v$  DII data as a function of dpa and He/dpa, fitted two ways (see below). The incubation  $dpa_i$ , taken as the  $f_v = 0$  intercept and  $f_v'$  the slope of fits of  $f_v(dpa)$  for various He/dpa. The  $dpa_i$  and  $f_v'$  as a function of He/dpa are cross-plotted and fitted in Figures 3c and d. Clearly,  $dpa_i$  generally decreases with the increasing He/dpa below He/dpa = 40, and is approximately constant at higher He/dpa.

As noted above, the  $dpa_i$  as a function of He/dpa was estimated in two ways [34]:  $dpa = g(f_v)$  and  $f_v = h(dpa)$ , where  $g$  and  $h$  are the linear fit equations [34]. Figure 3c shows linear fits to the av-



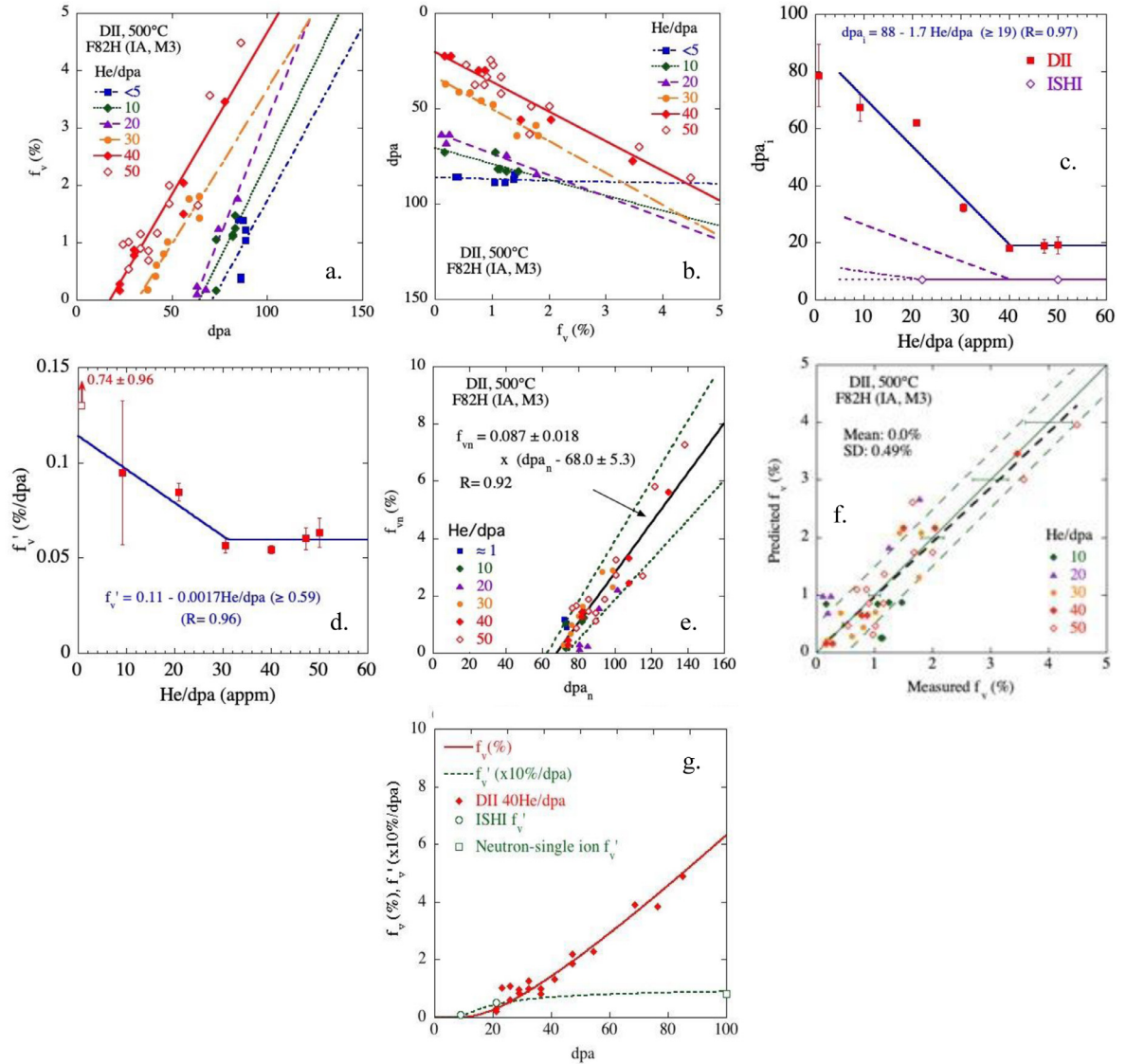


**Figure 3.** The high  $f_v$  data as a function of dpa fitted as: a)  $f_v(\text{dpa})$ ; and, b)  $\text{dpa}(f_v)$ ; c) a cross plot of the average  $\text{dpa}_i$  versus He/dpa for the two ways of fitting  $f_v(\text{dpa})$  and  $\text{dpa}(f_v)$ , with the solid fit line, and the ISHI  $\text{dpa}_i$  data extrapolated various ways (see text); d) the corresponding average  $f'_v$  versus He/dpa; e) all the  $f_v(\text{dpa})$  normalized to a common He/dpa = 10; f) a predicted versus measure  $f_v$  plot; and, g) sink bias evolution based  $f_v(\text{dpa})$  and  $f'_v(\text{dpa})$  models in comparison with the corresponding data.

average  $\text{dpa}_i$  estimates at  $\text{He/dpa} < 40$ . Thus, the average  $\text{dpa}_i$  versus He/dpa is represented by a hockey stick form as:

$$\text{dpa}_i = [88.1 \pm 8.0] - [1.72 \pm 0.29] (\text{He/dpa}) \quad (1\text{a})$$

$(10 \leq \text{He/dpa} < 40)$

$$\text{dpa}_i = 19.1 \pm 4.7 \quad (\text{He/dpa} \geq 40). \quad (1\text{b})$$

Here, the  $f'_v$  data are again fit in two ways:  $\text{dpa} = g(f_v)$  and  $f_v = h(\text{dpa})$  [34]. The  $f'_v$  data are scattered at some He/dpa, so we fit the average of the two estimates as shown in Figure 3e, as:

$$f'_v = [1.14 \pm 0.09] \times 10^{-1} - [1.76 \pm 0.41] \times 10^{-3} \text{He/dpa} \quad (2\text{a})$$

$(10 \leq \text{He/dpa} < 31)$

$$f'_v = 0.059 \pm 0.004 \quad (\text{He/dpa} \geq 31) \quad (2\text{b})$$

Equations 1 and 2 constitute a model for the DII  $f_v(\text{dpa}, \text{He/dpa})$  at 500°C. The model allows normalization of all of the DII  $f_v$  data

to any He/dpa condition. For example, for He/dpa of 50 and 10,  $\text{dpa}_i = 19$  and 71, and  $f'_v = 0.059$  and  $0.096\%/ \text{dpa}$ , respectively. Thus, a  $f_v = 3.6\%$  at He/dpa = 50 and 70 dpa (with a corresponding  $\text{dpa}-\text{dpa}_i = 51$ ) would be adjusted to a 122 dpa ( $= 51 + 71$ ) at He/dpa = 10, and the corresponding  $f_v$  adjusted by the  $f'_v$  ratio as  $3.6[0.096/0.059] = 5.9\%$ . The  $f_v$  for all of the high swelling data in this study, normalized to He/dpa = 10, are shown in Figure 3e. The normalized  $f_v$  data form a reasonably tight trend band. Figure 3f shows a corresponding predicted versus measured plot for the model.

Again, a more detailed and extended analysis of the DII data summarized here can be found in [34]. Briefly, the high  $\text{dpa}_i$  and the post  $\text{dpa}_i$  swelling rate in DII are both rationalized by simple defect partitioning to evolving defect sinks. The sinks include bubbles (b), voids (v), and dislocations (d) characterized by their sink strengths and sink biases for self-interstitials [34]. The initial bias of the dominant bcc lattice screw dislocations is for vacancies, rather than self-interstitials [23,24,70], and the initial bias of bubbles and voids ( $B_b, B_v$ ) is for self-interstitials, rather than being neutral [71,72]. The dislocation bias ( $B_d$ ) for self-interstitials in-

**Table 2**

The literature swelling data used in this study

Material	Irr. Type	Heat and/or Heat Treatment	T (°C)	dpa	Ref
T91	BOR60	30176, 1038°C/0.5h 760°C/0.5h	415	18.6	55
T91	HFIR	XA3590, 1040°C/0.5h 760°C/1h	400	36	51
T91	FFTF	30176, 1040°C/0.5h 760°C/0.5h	400–420	35–208	49, 52, 53
F82H	HFIR	Std., 1040°C/0.5h 760°C/2h	400	7.4–51	54
F82H	FFTF	Std., 1040°C/0.5h 760°C/2h	430	67	54
HT9	FFTF	91353, 1038/5m 760/0.5h	400–420	30–165	50
T91	Ion	n/a, 1038°C/0.5h 760°C/0.5h	475	137–548	38
HT9	Ion	“fusion” heat, 760/0.5h, 33%CW	480	200–600	41
Fe-9Cr	FFTF	1040°C/1h/AC 760°C/2h/AC	404–433	15 – 200	16,46–48
Fe-9Cr	EBR-II	1040°C/1h/AC 760°C/2h/AC	400–450	13 – 49	16,46
Fe-12Cr	FFTF	1040°C/1h/AC 760°C/2h/AC	404–433	15 – 200	16,46–48
Fe-12Cr	EBR-II	1040°C/1h/AC 760°C/2h/AC	400–450	13 – 49	16,46

creases as a population of edge dislocations builds up, partly due to climb of the screw dislocations into helical configurations with an edge component, and partly due to the formation of dislocation loops [70]. The cavities are initially bubbles, which have an interstitial bias that decreases sharply with their size [71,72].  $B_d - B_{b/v}$  starts at  $< 0$ , making void swelling impossible, but increases to  $> 0$  at  $\sim 7$  dpa. Thus, the dislocation and corresponding bias evolution effectively mediates the  $dpa_i$ . The  $B_d - B_{b/v}$  continues to increase to  $\sim 1.5\%$ , consistent with the observed post-incubation  $f_v' \approx 0.08\%/dpa$ . Figure 3f shows the good agreement between the bias evolution model predictions and the DII  $f_v$  data. This establishes a firm physical foundation for developing a predictive engineering swelling model for fusion-relevant irradiation conditions.

However, the data-rich DII data cannot alone be a basis for a fusion-relevant neutron swelling model. For example, the  $dpa_i$  are clearly much lower for ISHI versus those for DII at the same He/dpa, but there are results only for two He/dpa. The corresponding fusion relevant ISHI  $dpa_i$  as for a wider range of He/dpa were estimated in three ways. The first, shown by the dashed-dotted line in Figure 3c, is based on extrapolating from the  $dpa_i$  of  $\sim 7$  at He/dpa  $\approx 22$ , down to 5 dpa. Here we assume that the DII/ISHI  $dpa_i$  ratio of  $\sim 10$  at 22 dpa can be used to scale the ISHI data at lower He/dpa. The dashed line in Figure 3c is based on a similar DII/ISHI scaling, but starting at  $\sim 40$  dpa. The dotted line assumes that the approximately constant  $dpa_i$  between 22 and 50 dpa can be extrapolated to 5 He/dpa. Thus, the bounds for  $dpa_i$  at He/dpa = 10 are estimated to be between  $\sim 7$  and 26. Note, these large variations also partially account for uncertainties in the limited ISHI data.

Note, the DII results showing an estimated  $f_v$  of  $\sim 3\%$  at  $\sim 100$  dpa is significant, since this likely encompasses the allowable dimensional instability limits for fusion reactor structures [1]. Evaluation of  $f_v$  at higher dpa must rely on literature on fission neutron and, especially, single ion irradiation data.

**Literature neutron and single ion irradiation Data:** We also have collected swelling data from the literature [16,38–56] for various TMS and Fe-Cr model alloys for a range of irradiation conditions. This database currently consists of  $f_v$  (and usually  $N_v$  and  $\langle d_v \rangle$ ) for 95 neutron and 83 single ion irradiation data sets for F82H, 9Cr-Mo (T91), and HT9 as well as Fe-3 to 15Cr binary model alloys. The various types and sources of literature data used for the models below are summarized in Table 2. Key observations in the database analyses are summarized below for  $dpa_i$ ,  $f_v$ , and  $f_v'$ .

Figure 4 plots the single ion and fission neutron irradiation  $f_v$  data, as a function of dpa for: (a) Fe-9 and 12Cr model alloys; (b,d) 9Cr F82H and T91; and, (c,e) 12Cr HT9. Figure 4a shows neutron irradiation Fe-9Cr and Fe-12Cr data from Experimental Breeder Reactor – II (EBR-II) and Fast Flux Test Facility (FFTF) [16,46–48]. The nominal irradiation temperatures are between 400 to 430°C. Note, the DII data is for 500°C irradiations, in part to provide a temper-

ature adjustment to account for differences in the dpa rates [5,73]. In EBR-II, the  $dpa_i$  is very small for both binary alloys, while the  $dpa_i \approx 78 \pm 25$  dpa in FFTF. Garner et al. suggest that the difference may be due to different He generation rates of  $\sim 0.17$  versus  $\sim 0.02$  to 0.08 appm/dpa for EBR-II versus FFTF, respectively [56]. However, the post-incubation  $f_v'$  are similar, approaching  $\sim 0.1\%/dpa$  at  $f_v \approx 10\%$ . The fit lines for the fission neutron data in this study, shown in Figure 4a–c, all have the same  $f_v(dpa)$  curve shape for irradiations in different reactors (HFIR, FFTF, and BOR60) [16,46–55]: Fe-9–12Cr binary alloys (4a), T91 and F82H (4b) and HT9 (4c). The  $f_v(dpa)$  fit also has the same curve shape for single ion irradiations of T91 and HT9 in this study [38,41]. The nominal single ion irradiation temperatures were between 475 to 480°C. In all of these cases, the only difference between the various curves is the incubation  $dpa_i$ . The fitted fission neutron irradiation  $dpa_i$  is the smallest in the mixed spectrum HFIR, larger in the fast reactors (BOR60 and FFTF), and largest for the single ion irradiation. It is also notable that the  $dpa_i$  for T91 and F82H are the same for fission neutron irradiation in the same reactor. This is also the case for the single ion irradiation  $dpa_i$  for T91 and HT9. Figure 4d–e plots the  $f_v$  curves for single ion irradiated T91 and HT9 on an expanded scale, showing that  $f_v'$  continuously increases with dpa, reaching  $\sim 0.2\%/dpa$  at a very high dose of  $\sim 600$  dpa.

The common  $f_v(dpa-dpa_i)$  curve needs further confirmation, and is more approximate, especially with respect to some of the HT9 data at lower  $f_v$  and dpa. Further, the overlap of fission neutron and single ion irradiation data is limited to  $f_v < \sim 3\%$ . However, we consider the fitted TMS  $f_v(dpa-dpa_i)$  curve to be a reasonable representation of swelling in both cases.

A number of studies have pre-implanted various amounts of helium (generally at room temperature) followed by single ion irradiation at different temperatures [42–44,74–76]. Figure 5 shows examples of observed  $f_v$  vs. dpa trends. One notable result is that only small concentrations of  $\sim 10$  appm He are needed to promote void nucleation. However, compared to the dpa indexed common  $f_v$  curve shown as the solid line, 10 appm of pre-injected He greatly reduces  $f_v'$  in all cases. Pre-implantation of 100 appm He, leads to either  $f_v$  curves that further flatten, or that are fully suppressed. Clearly, He pre-implantation is not a good method to simulate helium effects. However, these data also clearly show that only a small amount of He is needed for void formation.

**Integrating the DII, ISHI, Fission Neutron, and Single Ion Irradiations  $f_v$  data to derive a fusion-relevant  $f_v(dpa, He/dpa)$  model:** A common  $f_v(dpa-dpa_i)$  curve can be derived by fitting the data shown in Table 2 and Figure 4. Again, the  $dpa_i$  strongly depends on the irradiation condition. In contrast,  $f_v$  vs. dpa (or  $f_v'$ ) trends are very similar for fission neutron T91 and F82H, as well as for single-ion irradiated T91 and HT9. Thus, all the  $f_v(dpa)$  data subsets shown in Figure 6a, were fit with a common  $f_v(dpa - dpa_i)$  fourth-order polynomial as shown in Figure 6b. The swelling rate,

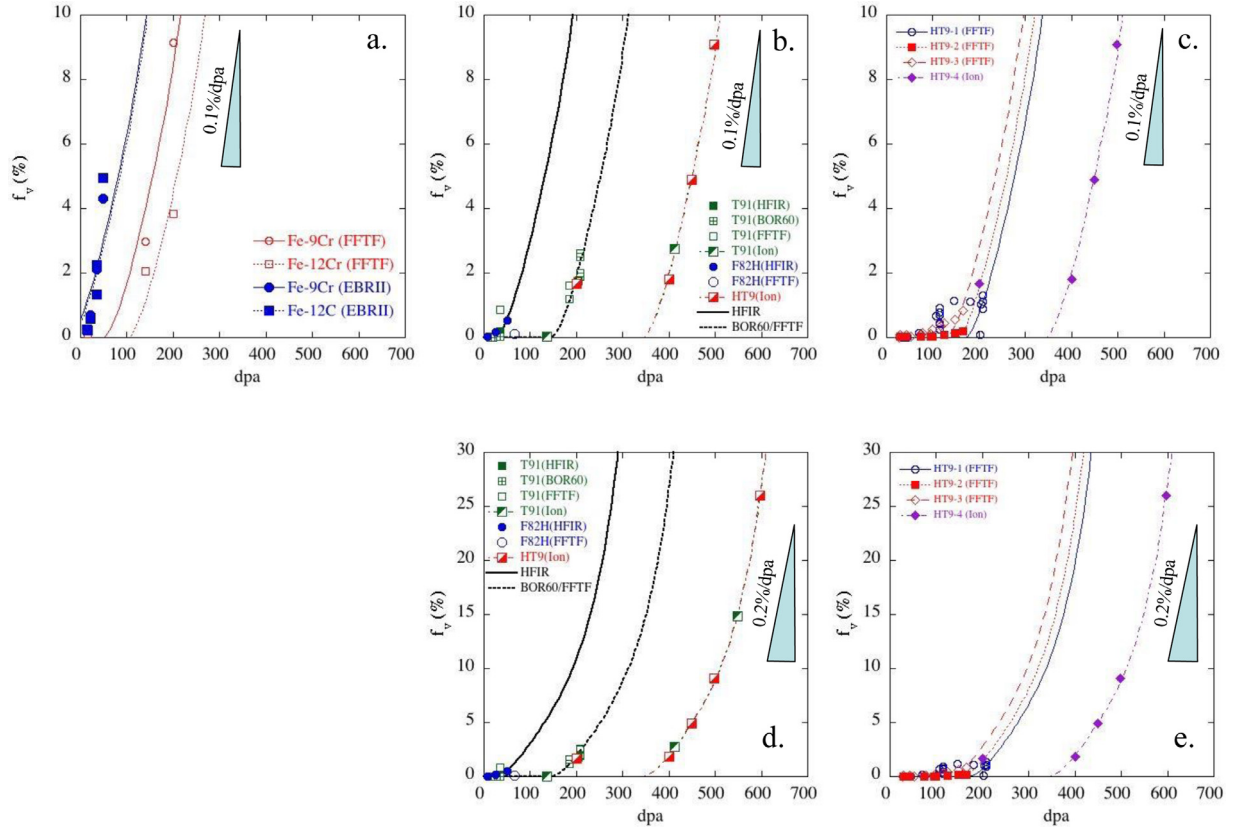


**Figure 4.** Swelling  $f_v$  vs dpa trends observed in the database for a) Fe-9,12Cr model alloys neutron irradiated in EBR-II and FFTF; b,d)  $\sim$  9Cr TMS (T91 and F82H) neutron irradiated in HFIR, FFTF, and BOR60 as well as single ion irradiated; and, c,e) various heats of HT-9 under neutron (FFTF) and single ion (Cr) irradiations. Note the single ion irradiation data have a common  $dpa_i \approx 350$  dpa.

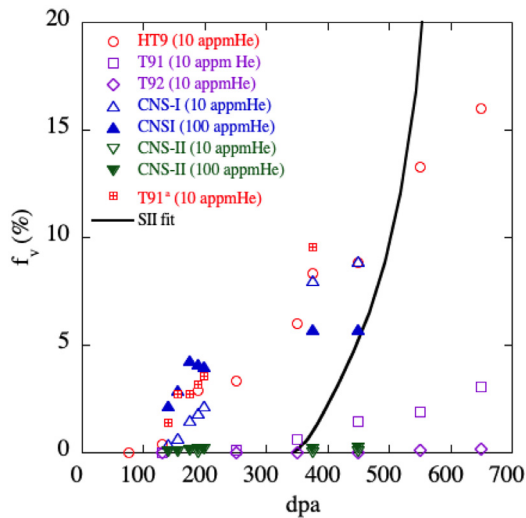


**Figure 5.** Swelling  $f_v(dpa)$  for various levels of He pre-injection, followed by single ion irradiations compared to the fitted single ion irradiation curve shown in Figures 4b to e.

$f_v'$ , increases with dpa up to slightly more than 0.2%/dpa between 200 to 250 dpa -  $dpa_i$ . The polynomial and the  $dpa_i$  values are summarized in the supplemental information, Equation SI1 and Table SI1. It is important to emphasize that the polynomial is only meant to represent the data, and in itself does not bear physical significance. The physical basis for the curve shape is discussed in Section 4.

A polynomial  $f_v(dpa - dpa_i)$  curve, now including the single ion, fission neutron, DII, and ISHI irradiation data, was refitted. The fit parameters are  $dpa_i$ , which are summarized in Table 3, and the polynomial swelling curve coefficients, which are given in Equation 3. Note, the model is supported by data only up to  $f_v \approx 26\%$ .

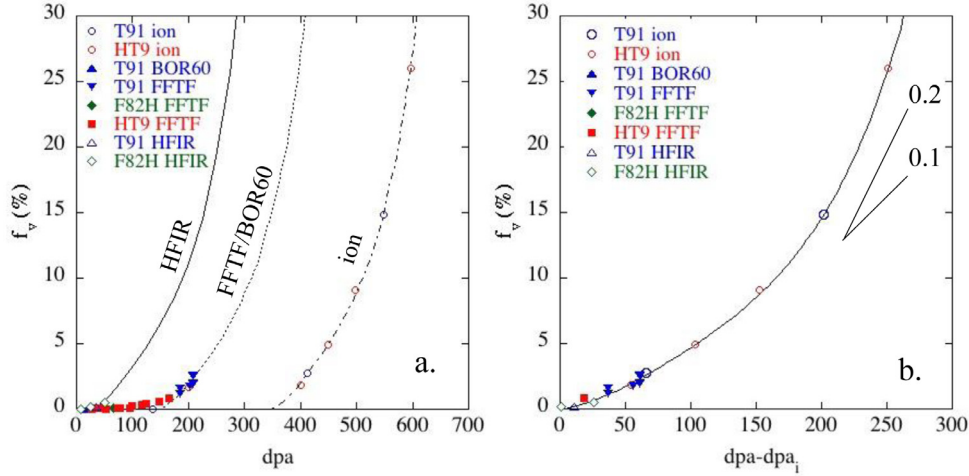
$$f_v = 2.06 \times 10^{-3}(dpa-dpa_i) + 1.32 \times 10^{-3}(dpa-dpa_i)^2 - 9.50 \times 10^{-6}(dpa-dpa_i)^3 + 2.50 \times 10^{-8}(dpa-dpa_i)^4 \quad (3)$$

Figure 7a shows  $f_v$  converted to a more common expression of swelling,  $S = f_v/(1-f_v)$ . For fusion relevant He/dpa = 10 neutron irradiations,  $dpa_i$  was taken as  $\sim 17 \pm 10$ , as described above (see Figure 3c). Note, the literature swelling data is all at lower temperatures than the DII and ISHI results at 500°C. The fact that the wide range of alloys and irradiation conditions result in similar  $S(dpa - dpa_i)$  curves is remarkable, and provides a basis for the proposed swelling model. Note the very high  $S$  and  $dpa$  data are entirely based on no helium, high dpa single ion irradiations, which may not be fully representative of fusion-relevant neutron irradiations. However, at lower  $S < \sim 10\%$ , the model predictions are much more robust, and largely based on the DII results discussed in detail in [34].

It is important to estimate the uncertainties of the nominal swelling curve in Figure 7b. The estimate for a higher swelling rate, shown as the dashed line, is based on a +50 % higher post-incubation  $f_v$  and  $dpa_i = 7$ . The lower swelling rate, shown by the dotted line, is based on a 50 % lower post-incubation  $f_v$  and a  $dpa_i = 26$ . Additional ISHI studies, especially at higher dpa, are critically needed to verify and refine these models.

**Table 3**  
Incubation  $dpa_i$  for various datasets in fitting to a common  $S(dpa - dpa_i)$

Irr. type	HFIR	FFTF/BOR60	Single Ion	DII	ISHI-22	ISHI-50
$dpa_i$	29.8	157	363	47.8	9.0	3.5
He/dpa	0.5 (F82H) 1 (T91)	0.04±0.02 (FFTF) 0.2 (BOR60)	0	10	22	50



**Figure 6.** a) Literature  $f_v$  data as a function of dpa for low He single ion and fission neutron irradiations, fitted with a fourth-order polynomial; and, b) the corresponding  $f_v(dpa - dpa_i)$  with a fitted  $dpa_i$ , for the same curve shape.

#### 4. Discussion

A fully detailed discussion of the issues for DII versus high helium neutron irradiations is beyond the scope of this paper, but is addressed further in [34]. We have shown that the ISHI and DII He/dpa on  $dpa_i$  and post-incubation  $f_v(dpa - dpa_i)$  data at 500°C are consistent with lower temperature single ion and fission neutron irradiation data, manifesting the same  $f_v(dpa - dpa_i)$  curve shape. While the polynomial curve is simply based on fitting available data sets, the physical basis for the post-incubation  $f_v$  curve is the partitioning of defects between evolving dislocation, bubble, and void sinks, resulting in a net self-interstitial dislocation bias of  $\sim 1$ –3%. As shown in Figure 3f [34], the bias evolution model predicts well the  $dpa_i$  and post-incubation  $f_v'$  in DII [34].

The same framework is used to model the single ion irradiation swelling data. While more details of the model can be found in [34], in summary,  $f_v'(dpa)$  for small  $B_d$ , and in the absence of bubble, is given by,

$$f_v' \approx G\eta B_d k_d k_v / [k_v + k_d]^2. \quad (4)$$

Here,  $k_v$  and  $k_d$  are void and dislocation sinks strengths,  $B_d$  is the net dislocation interstitial bias relative to voids,  $\eta$  is the defects/dpa, and  $G$  is the dpa generation rate. The  $f_v'$ ,  $B_d$ ,  $k_v$  and  $k_d$  all evolve with dpa. For example,  $k_v$  increases with an increasing number and/or size of voids. At the same time, the interstitial bias for voids decreases with size, approaching 0. However, the interstitial bias for dislocations may continue to increase, as loops and edge network components develop with increasing dpa. In this case, the net dislocation versus void interstitial bias also increases. Further, initially  $k_v$  is much less than  $k_d$ . However, the increase in size and number of voids increases  $k_v$ . For a given  $B_d$ , the maximum  $f_v' = G\eta B_d / 4$  when  $k_v = k_d$ . Thus,  $f_v'$  increases with dpa, approaching this maximum. There are a variety of ways of modeling the increases in  $B_d$ ,  $k_v$  and  $k_d$ , but all give roughly similar predictions of the shape of the  $f_v(dpa - dpa_i)$  curve. The model shown in Figures 8a–d is based on the following steps.

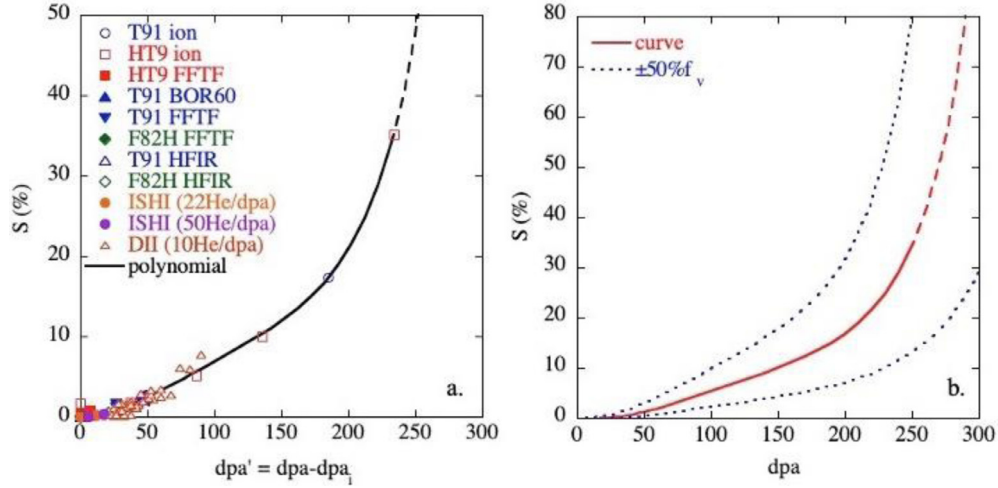
- The average radius,  $r_v$ , of a constant number of voids,  $N_v$ , increases with  $f_v$  and is used to calculate the void sink strength,  $k_v$ , and net dislocation minus void interstitial bias,  $B_d$ .
- The nearly saturated edge dislocation density (including loops) slowly increases with dpa, and is used to calculate the dislocation sink strength,  $k_d$ , and net interstitial  $B_d$ .
- The increases in the net dislocation interstitial bias,  $B_d$ , and the  $k_v/k_d$  sink strength ratio with dpa are used to calculate  $f_v'(dpa)$ ,

Figure 8a shows the fit to the single ion data at high dpa for the very reasonable parameters listed in Table 4 as Case 1. The sink strengths and biases are shown in Figure 8b. Figure 8c shows the predictions for an alternative evolution model, where  $N_v$  and  $r_v$  both increase with dpa, consistent with the increasing  $f_v$ . The corresponding sink strengths and biases are shown in Figure 8d. The predictions of both model variants are compared to the  $f_v(dpa - dpa_i)$  polynomial curve in Figure 9.

As discussed in [34], the DII model sink and bias parameters for  $dpa_i$  and  $f_v'$  also must be consistent at the onset of swelling. For purposes of the DII data analysis, we have taken the void transition to occur at a bubble size  $d_c \approx 4$  nm. This so-called critical size is often observed as the pinch-off size in a bimodal bubble (small)-void (larger and growing) cavity distribution. We have shown that the results of the DII analysis are not sensitive to the exact value of  $d_c$  [34], which has been widely observed to be in the range of  $\sim 2.5$ –5 nm for both neutrons and ions [13, 55,77–79]. A detailed multiscale model has shown to be consistent with the ISHI data including both  $dpa_i$  and  $f_v'$  [68,69], as shown in supplemental information, SI2. Examples of observed pinch-off  $d_c$  for ions and neutrons are also shown in SI2. Note, the typical  $d_c$  for ISHI neutrons is slightly smaller than for ions, at  $\sim 2.5$  nm [32].

Of course, it will be critical to carry out additional experimental and modeling studies to refine, extend, and ultimately validate the swelling model. A major near-term focus should be extending ISHI irradiations to higher dpa over a range of temperatures and He/dpa ratios. The US-Japan JP28-29 experiment in HFIR had that objective, but was not successful due to loss of temperature control





**Figure 7.** a) A polynomial  $f_v(dpa - dpa_i)$  refitted to all the  $f_v$  data and converted to swelling as  $S = f_v/(1-f_v)$ ; and, b) a  $S(dpa)$  prediction for fusion reactor relevant irradiation condition of He/dpa = 10, along with estimated uncertainties. The dashed lines are beyond the available data range.

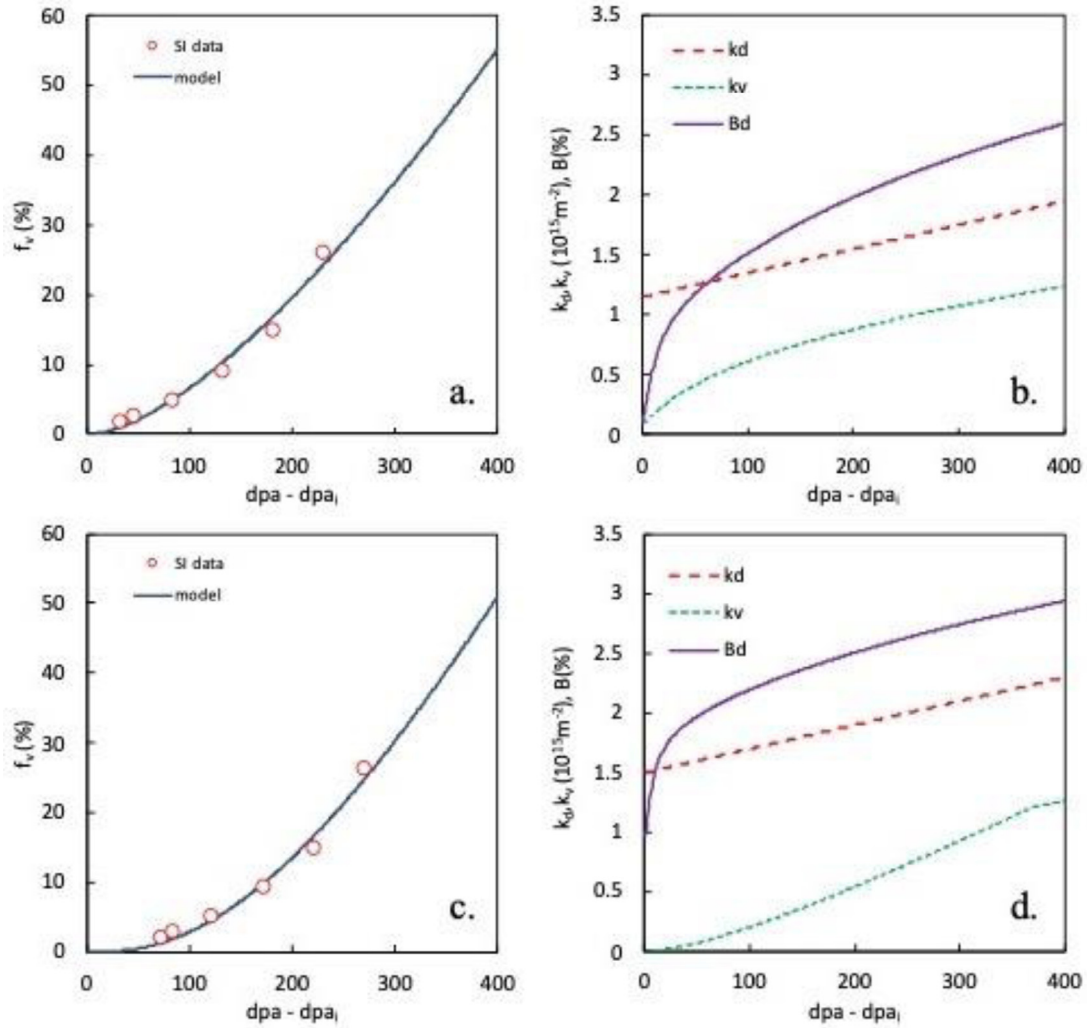


**Figure 8.** a)  $f_v$  versus  $dpa - dpa_i$  model based on the defect partitioning on evolving sinks, fitted to the single ion data at high dpa for the parameters listed in Table 4; b) the corresponding sink strengths and biases; c) and, d) the same plots for the alternative evolution model, where  $N_v$  and  $r_v$  both increase with dpa.

**Table 4**  
The parameters for the single ion swelling models shown in Figures 8 and 9

Property	Parameter	unit	Case 1	Case 2
Dislocation properties				
Initial dislocation density	$\rho_{\text{initial}}$	$\text{m}^{-2}$	$4 \times 10^{14}$	$4 \times 10^{14}$
Initial SD* fraction	$\rho_{\text{SD}}/\rho_{\text{initial}}$		1	1
ED* density plateau (saturation)	$\rho_{\text{ED,max}}$	$\text{m}^{-2}$	$1.15 \times 10^{15}$	$1.5 \times 10^{15}$
ED plateau slope	$\Delta\rho_{\text{ED,max}}/\Delta\text{dpa}$	$\text{m}^{-2}$	$2 \times 10^{12}$	$2 \times 10^{12}$
$\rho_{\text{ED}}$ saturation constant	$\text{dpa}_0$	dpa	8	8
Void properties				
Initial density	$N_{\text{v,ini}}$	$\times 10^{21} \text{m}^{-3}$	2.7	0.01
Maximum (saturation) density	$N_{\text{v,max}}$	$\times 10^{21} \text{m}^{-3}$	2.7	2.9
Density increment rate per dpa	$\Delta N_{\text{v}}/\Delta\text{dpa}$	$\times 10^{21} \text{m}^{-3}/\text{dpa}$	0	0.0079
Cavity SIA interaction distance	$\delta$	Nominal $\delta_{\text{n}}$	0.43	0.43
Incubation dpa	$\text{dpa}_i$	dpa	367.	328

\*SD: Screw dislocations; ED: edge dislocations.

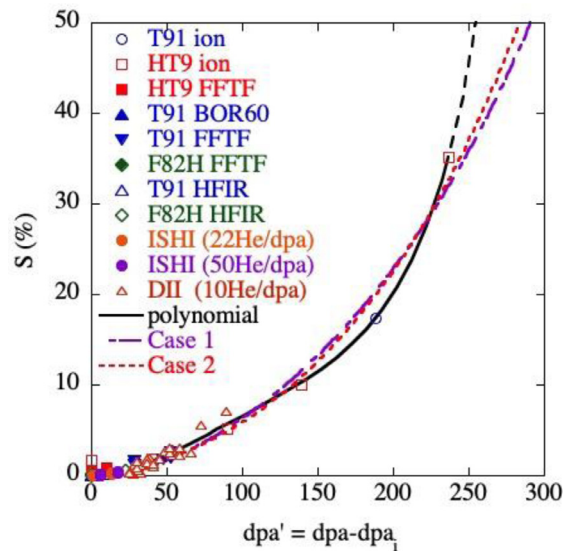


**Figure 9.** Two bias evolution-based models compared to the data and to the polynomial model.

[32, 80]. However, re-irradiation of existing alloys from the previous ISHI 9 (JP26) and 21 (JP27) dpa irradiation conditions could reach 40 dpa in several years. There is also an opportunity to use ions to re-irradiate the ISHI alloys, again to reach higher dpa (and He) in what has been described as the bootstrapping experiments [81]. Bootstrapping would compare the effects of ISHI irradiations, to a series DII increments, with both reaching a common higher dpa and He. For example, ion re-irradiations of ISHI 9 dpa specimens, from the JP26 experiment, would be carried out to match the ISHI conditions in the JP27 experiment at 22 dpa. DII of the 22 dpa JP27 irradiation would match the conditions at 40 dpa for the new ISHI reirradiations. The bootstrapping approach is schematically illustrated in Figure 10. Notably, these experiments would exploit lab-on-a-chip miniaturization techniques and, ideally, would involve dedicated lower dpa rate, extended time ion irradiations, to avoid confounding dose rate effects, like enhanced recombination, at lower temperatures.

Special experiments to gain insight on key mechanisms, such as injected interstitial effects, recombination, cavity and dislocation evolutions and the corresponding effects on self-interstitial bias would be part of an overall roadmap for developing rigorous physical models of the swelling in He-rich fusion environments. Finally, in the near future, a multiscale master model of helium and defect generation, transport, fate and consequences will be updated to reflect the recent insights, gained in this and ongoing experimental studies.

## 5. Summary

Equation 3 and the ISHI  $\text{dpa}_i$  vs. He/dpa relation in Figure 3c constitute a TMS void swelling model that can be, and has been, used in engineering analysis of the dimensional stability of fusion structures [1]. The reliability of the  $f_v'$  model at  $\leq 150$  dpa largely rests on the DII data, which is also used along with the ISHI results to estimate the fusion relevant  $\text{dpa}_i$ . Notably, both the trends in  $\text{dpa}_i$  with He/dpa and the post-incubation  $f_v'$ , which is mediated by simple defect partitioning between sinks with different biases, are physically reasonable and can be modeled. However, as discussed in [34], the model is far from the last word on the swelling of TMS in fusion environments, and much more research is needed for verification and refinement, including an extension to lower temperatures. This research will also involve development of a detailed multiscale master model [2,67,68], acquiring higher dpa ISHI data, and further resolution of DII issues, in part based on advanced approaches to minimizing the corresponding artifacts. A more detailed treatment of physics not included in the data-driven model, like the evolution of dislocations structures and sink biases, is very critical. It is also important to model the effect of higher helium on other microstructural evolutions, especially dislocation loops. Of course, the models ultimately must be validated by irradiations in a high-energy neutron source.

## CRedit author statement

**Takuya Yamamoto:** Conceptualization, Methodology, Software, Investigation, Formal analysis, Writing-Original Draft, Writing-Review & Editing. **G. Robert Odette:** Conceptualization, Methodology, Validation, Formal analysis, Project administration, Funding acquisition, Writing-Original Draft, Writing-Review & Editing.

## Declaration of Competing Interest

The authors declare that they have no known competing financial interests or personal relationships that could have appeared to influence the work reported in this paper.

## Data Availability

Data will be made available on request.

## Acknowledgments

The authors gratefully acknowledge a large number of collaborators who helped in carrying out the irradiation experiments and PIE microstructural characterization studies. They include: Drs. Y. Wu and P. Miao at UCSB (TEM); Drs. D.J. Edwards, R.J. Kurtz, D.S.

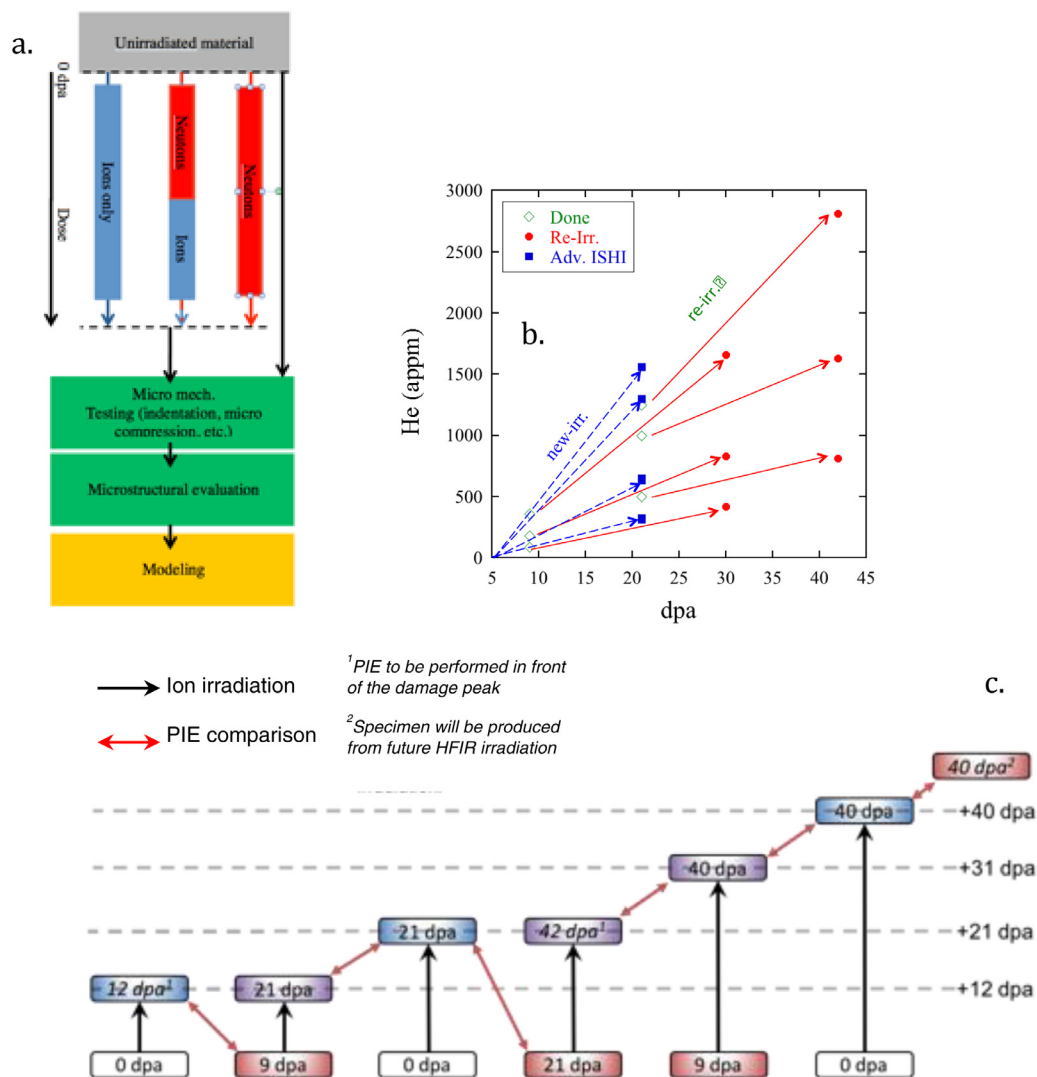


**Figure 10.** Schematic illustrations of: a) the neutron-ion irradiations bootstrapping approach to probe very high dose phenomena at a lower cost and in a shorter time; b) expected He-dpa conditions in re-irradiation of ISHI JP26 and 27 specimens; and, c) an approach of neutron-single ion irradiation bootstrapping using ISHI JP26 and JP27 specimens.

Gelles, H.J. Jung, K. Kruska at PNNL for PIE (specimen preparation and TEM); Professors K. Yabuuchi, S. Kondo, A. Kimura and Mr. Hashitomi at the Kyoto University DuET facility (DII); Drs. R.E. Stoller and Y. Katoh at ORNL (ISHI HFIR irradiations and specimen recovery and shipping); Dr. J. Haley at Oxford University (DuET TEM PIE while visiting UCSB). This work was supported by the U.S. Department of Energy, Office of Fusion Energy Sciences, under the contract DE-FG03-94ER54275. The Joint Research Program on Zero-Emission Energy Research Institute of Advanced Energy, at Kyoto University, supported the DuET irradiation experiments. The TEM PIE microstructural characterizations were carried out in the NSF supported UCSB California Nanosystems Microstructural and Microanalysis, in the DOE/INL supported National Scientific User CAES facility operated by Idaho State University and at International Research Center for Nuclear Materials Science, Tohoku University (Oarai, Japan).

### Supplementary materials

Supplementary material associated with this article can be found, in the online version, at [doi:10.1016/j.jnucmat.2022.154085](https://doi.org/10.1016/j.jnucmat.2022.154085).

### References

- [1] A. Ghazari, R. Forte, T. Yamamoto, G.R. Odette, N. Ghoniem, Radiation effects on stress evolution and dimensional stability of large fusion energy structures, *Fusion Eng. Des.* 172 (2021) 112756.
- [2] Y. Dai, G.R. Odette, T. Yamamoto, The Effects of helium on irradiated structural alloys, *Comprehensive Nuclear Materials*, R. Konings, T. R. Allen, R. E. Stoller, S. Yamanaka Eds., Elsevier, 2012.
- [3] C. Cawthorne, E.J. Fulton, Voids in irradiated stainless steel, *Nature* 216 (1967) 575.
- [4] H. Trinkaus, B.N. Singh, Helium accumulation in metals during irradiation – where do we stand? *J. Nucl. Mater.* 323 (2003) 229.
- [5] L.K. Mansur, Theory and experimental background on dimensional changes in irradiated alloys, *J. Nucl. Mater.* 216 (1994) 97.
- [6] G.R. Odette, S.C. Langley, Modeling of synergistic effects of displaced atom and transmutant helium damage in fission and fusion environment, in: *Proceedings of the First International Conference on Radiation Effects & Tritium Technology for Fusion Reactors*, ANS, 1976, p. 395.
- [7] G.R. Odette, Modeling microstructural evolution under irradiation, *J. Nucl. Mater.* 85–86 (1979) 533.
- [8] G.R. Odette, P.J. Mazaisz, J.A. Spitznagel, Fission fusion correlations for swelling and microstructure in stainless steels: the effect of the helium to displacement per atom ratio, *J. Nucl. Mater.* 103&104 (1981) 1289.
- [9] G.R. Odette, R.E. Stoller, A theoretical assessment of the effect of microchemical microstructural and environmental mechanisms on swelling incubation in austenitic stainless steels, *J. Nucl. Mater.* 122&123 (1984) 514.
- [10] G.R. Odette, Modeling microstructural evolution in fusion reactor environment, *J. Nucl. Mater.* 133&134 (1985) 127.

- [11] R.E. Stoller, G.R. Odette, A composite model of microstructural evolution in austenitic stainless steel under fast neutron irradiation, in: 13th International Symposium on the Influence of Irradiation on Material Properties, ASTM STP-955, ASTM, 1987, p. 371.
- [12] R.E. Stoller, G.R. Odette, A comparison of the relative importance of helium and vacancy accumulation in void nucleation, in: 13th International Symposium on the Influence of Irradiation on Material Properties, ASTM STP-955, ASTM, 1987, p. 358.
- [13] G.R. Odette, On mechanisms controlling swelling in ferritic alloy and martensitic alloys, *J. Nucl. Mater.* 155-157 (1988) 921.
- [14] R.E. Stoller, Microstructural Evolution in Fast Neutron Irradiated Austenitic Stainless Steels, PhD Thesis Univ. Cal. Santa Barb., 1987 and ORNL, 1988.
- [15] R.E. Stoller, G.R. Odette, Analytical solutions for helium bubbles and critical radius parameters using a hard sphere equation of state, *J. Nucl. Mater.* 131 (1985) 118.
- [16] F.A. Garner, M.B. Toloczko, B.H. Sencer, Comparison of swelling and irradiation creep behavior of fcc-austenitic and bcc-ferritic/martensitic alloys at high neutron exposure, *J. Nucl. Mater.* 376 (2000) 123.
- [17] Y. Katoh, Y. Kohno, A. Kohyama, Dual-ion irradiation effects on microstructure of austenitic alloys, *J. Nucl. Mater.* 205 (1993) 354.
- [18] Y. Katoh, R.E. Stoller, Y. Kohno, A. Kohyama, The influence of He/dpa ratio and displacement rate on microstructural evolution: a comparison of theory and experiment, *J. Nucl. Mater.* 210 (1994) 290.
- [19] G.R. Odette, Recent progress in developing and qualifying nanostructured ferritic alloys for advanced fission and fusion applications, *JOM* 66 (2014) 2427.
- [20] J.J. Sniegowski, W.G. Wolfer, On the physical basis for the swelling resistance of ferritic steels, in: Proc. Topical Conf. on Ferritic Alloys for Use in Nuclear Energy Technologies, AIME, 1984, p. 579.
- [21] R. Bullough, H.M. Wood, E.A. Little, A microstructural explanation for the low swelling of ferritic steels, Effects of Irradiation on Materials. D. Kramer, H.R. Brager and J.S. Perrin eds. ASTM STP 725 (1981) 593.
- [22] E.A. Little, R. Bullough, H.M. Wood, On the swelling resistance of ferritic steel, *Proc. R. Soc. London A372* (1980) 565.
- [23] W.G. Wolfer, The Dislocation Bias, *J. Comput.-Aided Mater. Des.* 14 (2007) 403.
- [24] Z. Chang, D. Terentyev, N. Sandberg, K. Samuelsson, P. Olsson, Anomalous bias factors of dislocations in bcc iron, *J. Nucl. Mater.* 461 (2015) 221.
- [25] A. Kimura, R. Kasada, K. Morishita, R. Sugano, A. Hasegawa, K. Abe, T. Yamamoto, H. Matsui, N. Yoshida, B.D. Wirth, T.D. Rubia, High resistance to helium embrittlement in reduced activation martensitic steels, *J. Nucl. Mater.* 307-311 (2002) 521.
- [26] T. Yamamoto, G.R. Odette, L.R. Greenwood, An in-situ helium implantation approach to irradiations with controlled He/dpa ratios at fusion relevant conditions, *Fusion Materials Semiannual Report 1/1 to 6/30/2005 DOE/ER-313/38* (2005) 95.
- [27] T. Yamamoto, G.R. Odette, P. Miao, D.T. Hoelzer, J. Bentley, N. Hashimoto, H. Tanigawa, R.J. Kurtz, The transport and fate of helium in nanostructured ferritic alloys at fusion relevant He/dpa ratios and dpa rates, *J. Nucl. Mater.* 367-370 (2007) 399.
- [28] R.J. Kurtz, G.R. Odette, T. Yamamoto, D.S. Gelles, P. Miao, B.M. Oliver, The transport and fate of helium in martensitic steels at fusion relevant He/dpa ratios and dpa rates, *J. Nucl. Mater.* 367-370 (2007) 417.
- [29] G.R. Odette, M.J. Alinger, B.D. Wirth, Recent developments in irradiation-resistant steels, *Annu. Rev. Mater. Res.* 38 (2008) 471.
- [30] T. Yamamoto, G.R. Odette, P. Miao, D.J. Edwards, R.J. Kurtz, Helium effects on microstructural evolution in tempered martensitic steels: in situ helium implantation studies in HFIR, *J. Nucl. Mater.* 386-388 (2009) 338.
- [31] G.R. Odette, P. Miao, D.J. Edwards, T. Yamamoto, R.J. Kurtz, Y. Tanigawa, Helium transport, fate and management in nanostructured ferritic alloys: in situ helium implantation studies, *J. Nucl. Mater.* 417 (2011) 1001.
- [32] T. Yamamoto, Y. Wu, G.R. Odette, D. Edwards, R. Kurtz, Microstructure evolution in tempered martensitic steels under in-situ helium injection experiment in HFIR JP28/29, *Fusion Materials Semiannual Report 12/31/2015 DOE/ER-313/59* (2016) 15.
- [33] G.R. Odette et al. (personal communication)
- [34] T. Yamamoto, Y. Wu, K. Yabuuchi, J. Haley, K. Yoshida, A. Kimura, G.R. Odette, Cavity evolution and void swelling in dual ion irradiated tempered martensitic steels, submitted to *J. Nucl. Mater.* (2022).
- [35] T. Yamamoto, Y. Wu, G.R. Odette, K. Yabuuchi, S. Kondo, A. Kimura, A dual ion irradiation study of helium-dpa interactions on cavity evolution in tempered martensitic steels and nanostructured ferritic alloys, *J. Nucl. Mater.* 449 (2014) 190.
- [36] T. Yamamoto, Y. Wu, G.R. Odette, K. Yabuuchi, S. Kondo, A. Kimura, "On the effects of helium-dpa interactions on cavity evolution in tempered martensitic steels under dual ion-beam irradiation," *Fusion Materials Semiannual Report 6/30/2015 DOE/ER-313/58* (2015) 12.
- [37] T. Yamamoto, Y. Wu, G.R. Odette, K. Yabuuchi, S. Kondo, A. Kimura, "On the effects of helium-dpa interactions on cavity evolution in tempered martensitic steels under dual ion-beam irradiation," *Fusion Materials Semiannual Report 6/30/2016 DOE/ER-313/60* (2016) 12.
- [38] J.G. Gigax, T. Chen, Hyosim Kim, L.M. Price, J. Wang, E. Aydogan, S.A. Maloy, D.K. Schreiber, M.B. Toloczko, F.A. Garner, L. Shao, Radiation response of alloys T91 at damage levels up to 1000 peak dpa, *J. Nucl. Mater.* 482 (2016) 257.
- [39] J.G. Gigax, H. Kim, T. Chen, F.A. Garner, L. Shao, Radiation instability of equal channel angular extruded T91 at ultra-high damage levels, *Acta Mater.* 132 (2017) 395.
- [40] Y. Li, T. Shen, X. Gao, C. Yao, K. Wei, J. Sun, B. Li, Y. Zhu, L. Pang, M. Cui, H. Chang, J. Wang, H. Zhu, B. Hu, Z. Wang, Cavity swelling in three ferritic-martensitic steels irradiated by 196 MeV Kr ions, *Chin. Phys. Lett.* 30 (2013) 126101.
- [41] F.A. Garner, L. Shao, M.B. Toloczko, S.A. Malloy, V.N. Voyevodin, "Use of self-ion bombardment to study void swelling in advanced radiation-resistant alloys," Proc. 17th Int. Conf. on Environmental Degradation of Materials in Nuclear Power Systems Aug.9-13, 2015, Ottawa, Ontario, Canada.
- [42] Xu Wang, Qingzhi Yan, Gary S. Was, Lumin Wang, Void swelling in ferritic-martensitic steels under high dose ion irradiation: Exploring possible contributions to swelling resistance, *Scr. Mater.* 112 (2016) 9.
- [43] E. Getto, K. Sun, S. Taller, A.M. Monterrosa, Z. Jiao, G.S. Was, Methodology for determining void swelling at very high damage under ion irradiation, *J. Nucl. Mater.* 477 (2016) 273.
- [44] E. Getto, K. Sun, A.M. Monterrosa, Z. Jiao, M.J. Hackett, G.S. Was, Void swelling and microstructure evolution at very high damage level in self-ion irradiated ferritic-martensitic steels, *J. Nucl. Mater.* 480 (2016) 159.
- [45] D.S. Gelles, Microstructural development in reduced activation ferritic alloys irradiated to 200 dpa at 420°C, *J. Nucl. Mater.* 212-215 (1994) 714.
- [46] D.S. Gelles, Microstructural examination of neutron-irradiated simple ferritic alloys, *J. Nucl. Mater.* 108&109 (1982) 515.
- [47] Y. Katoh, A. Kohyama, D. Gelles, Swelling and dislocation evolution in simple ferritic alloys irradiated to high fluence in FFTF/MOTA, *J. Nucl. Mater.* 225 (1995) 154-162.
- [48] D.S. Gelles, Void swelling in binary Fe-Cr alloys at 200 dpa, *J. Nucl. Mater.* 225 (1995) 163.
- [49] M.B. Toloczko, F.A. Garner, C.R. Eiholzer, Irradiation creep and swelling of the US fusion heats of HT9 and 9Cr-1Mo to 208 dpa at  $\approx 400^\circ\text{C}$ , *J. Nucl. Mater.* 212-215 (1994) 604.
- [50] M.B. Toloczko, F.A. Garner, Irradiation creep and void swelling of two LMR heats of HT9 at  $\approx 400^\circ\text{C}$  and 165 dpa, *J. Nucl. Mater.* 233-237 (1996) 289.
- [51] J.M. Vitek, R.L. Klueh, Microstructure of 9Cr-1MoV Nb steel irradiated to 36 dpa at elevated temperatures in HFIR, *J. Nucl. Mater.* 122&123 (1984) 254.
- [52] J.J. Kai, R.L. Klueh, Microstructural analysis of neutron-irradiated martensitic steels, *J. Nucl. Mater.* 230 (1996) 116.
- [53] J. Van den Bosch, O. Anderoglu, R. Dickerson, M. Hartl, P. Dickerson, J.A. Aguiar, P. Hosemann, M.B. Toloczko, S.A. Maloy, SANS and TEM of ferritic-martensitic steel T91 irradiated in FFTF up to 184 dpa at 413°C, *J. Nucl. Mater.* 440 (2013) 91.
- [54] E. Wakai, N. Hashimoto, Y. Miwa, J.P. Robertson, R.L. Klueh, K. Shiba, S. Jitsukawa, Effect of helium production on swelling of F82H irradiated in HFIR, *J. Nucl. Mater.* 283-287 (2000) 799.
- [55] Z. Jiao, S. Taller, K. Field, G. Yeli, M.P. Moody, G.S. Was, Microstructure evolution of T91 irradiated in the BOR60 fast reactor, *J. Nucl. Mater.* 504 (2018) 122.
- [56] F.A. Garner, D.S. Gelles, L.R. Greenwood, T. Okita, N. Sekimura, W.G. Wolfer, Synergistic influence of displacement rate and helium/dpa ratio on swelling of Fe-(9,12)Cr binary alloys in FFTF at  $\sim 400^\circ\text{C}$ , *J. Nucl. Mater.* 329-333 (2004) 1008.
- [57] K. Shiba, M. Enoda, S. Jitsukawa, Reduced activation martensitic steels as a structural material for ITER test blanket, *J. Nucl. Mater.* 329-333 (2004) 243.
- [58] K. Shiba, H. Tanigawa, T. Hirose, T. Nakata, Development of the toughness-improved reduced-activation F82H steel for DEMO reactor, *Fusion Sci. Technol.* 62 (1) (2012) 145. doi:10.13182/FST12-A14127.
- [59] H.E. Hofmans, "Tensile and impact properties of Eurofer97 plate and bar," NRG Report 20023/00.38153/P (2000) Petten, The Netherlands.
- [60] S.J. Zinkle, L.L. Snead, Opportunities and limitations for ion beams in radiation effects studies: bridging critical gaps between charged particle and neutron irradiations, *Scr. Mater.* 143 (2018) 154.
- [61] F.A. Garner, Impact of the injected interstitial on the correlation of charged particle and neutron-induced radiation damage, *J. Nucl. Mater.* 117 (1983) 177.
- [62] Lin Shao, C.-C. Wei, J. Gigax, A. Aitkaliyeva, D. Chen, B.H. Sencer, F.A. Garner, Effect of defect imbalance on void swelling distributions produced in pure iron irradiated with 3.5MeV self-ions, *J. Nucl. Mater.* 453 (2014) 176.
- [63] A.D. Brailsford, L.K. Mansur, Effect of self-ion injection in simulation studies of void swelling, *J. Nucl. Mater.* 71 (1977) 110.
- [64] D.L. Plumton, H. Attaya, W.G. Wolfer, Conditions for the suppression of void formation during ion-bombardment, *J. Nucl. Mater.* 122&123 (1984) 650.
- [65] D.L. Plumton, G.L. Klucinski, The magnitude and distribution of the excess interstitial fraction during heavy ion irradiation, *J. Nucl. Mater.* 133&134 (1985) 444.
- [66] M.P. Short, D.R. Gaston, M. Jin, L. Shao, F.A. Garner, Modeling injected interstitial effects on void swelling in self-ion irradiation experiments, *J. Nucl. Mater.* 471 (2016) 200.
- [67] B. Michaut, T. Jourdan, J. Malaplate, A. Renault-Laborne, F. Sefta, B. Decamps, Cluster dynamics modeling and experimental investigation of the effect of injected interstitials, *J. Nucl. Mater.* 496 (2017) 166.
- [68] T. Yamamoto, G.R. Odette, R.J. Kurtz, B.D. Wirth, "A multi-scale model of helium transport and fate in irradiated tempered martensitic steels and nanostructured ferritic alloys," *Fusion Materials Semiannual Report 12/31/2010 DOE/ER-0313/49* (2011) 73.
- [69] T. Yamamoto and G.R. Odette, "A multi-scale model of helium transport, fate and consequences in irradiated tempered martensitic steels: void swelling and dpa rate effects," *Fusion Materials Semiannual Report 6/30/2019 DOE/ER-0313/66* (2019) 169.
- [70] J.C. Haley, F. Liu, E. Tarleton, A.C.E. Cocks, G.R. Odette, S. Lozano-Perez, S.G. Roberts, Helical dislocations: observation of vacancy defect bias of screw dislocations in neutron irradiated Fe-9Cr, *Acta Mater.* 181 (2019) 173.



- [71] M.P. Surh, W.G. Wolfer, Accurate mean field void bias factors for radiation swelling calculations, *J. Comput.-Aided Mater. Des.* 14 (2007) 419.
- [72] A.A. Kohnert, M.A. Cusentino, B.D. Wirth, Molecular statics calculations of the biases and point defect capture volumes of small cavities, *J. Nucl. Mater.* 499 (2018) 460.
- [73] L.K. Mansur, Correlation of neutron and heavy ion damage, *J. Nucl. Mater.* 78 (1978) 156.
- [74] Z. Jiao, N. Ham, G.S. Was, Microstructure of helium-implanted and proton-irradiated T91 ferritic/martensitic steel, *J. Nucl. Mater.* 367-370 (2007) 440.
- [75] Xu Wang, Anthony M. Monterrosa, Feifei Zhang, Hao Huang, Qingzhi Yan, Zhi-jie Jiao, Gary S. Was, Lumin Wang, Void swelling in high dose ion-irradiated reduced activation ferritic-martensitic steels, *J. Nucl. Mater.* 463 (2015) 119.
- [76] A.M. Monterrosa, Z. Jiao, G.S. Was, The influence of helium on cavity evolution in ion-irradiated T91, *J. Nucl. Mater.* 509 (2018) 707.
- [77] S. Taller, G. VanCoeveing, B.D. Wirth, G.S. Was, Predicting structural material degradation in advanced nuclear reactors with ion irradiation, *Sci. Rep.* 11 (2021) 2949.
- [78] S. Taller, Z. Jiao, K. Field, G.S. Was, Emulation of fast reactor irradiated T91 using dual ion beam irradiation, *J. Nucl. Mater.* 527 (2019) 151831.
- [79] D. Woodley, S. Taller, Z. Jiao, K. Sun, G.S. Was, The Role of Co-injected helium on swelling and cavity evolution at high damage levels in ferritic-martensitic steels, *J. Nucl. Mater.* 530 (2021) 152912.
- [80] H. Sakasegawa, T. Hirose, X. Chen, J.W. Geringer, Y. Katoh, "Irradiation hardening behavior of F82H in JP28 and 29," *Fusion Materials Semiannual Report* 6/30/2017 DOE/ER-313/62 (2017) 3.
- [81] T. Yamamoto, G.R. Odette, P.B. Wells, D.J. Edwards, K. Kruska, R.J. Kurtz, S.J. Tumey, "Designs and specimen matrices for re-irradiation of ISHI samples in HFIR Rabbit capsule along with neutron-ion bootstrapping experiments," *Fusion Materials Semiannual Report* 12/31/2018 DOE/ER-313/65 (2019) 139.